

# Selective Phosphorylation of AMPA Receptor Contributes to the Network of Long-Term Potentiation in the Anterior Cingulate Cortex

Qian Song,<sup>1\*</sup> Hong-Wei Zheng,<sup>2\*</sup>  Xu-Hui Li,<sup>1</sup>  Richard L. Huganir,<sup>3</sup>  Thomas Kuner,<sup>2</sup>  Min Zhuo,<sup>1,4</sup> and  Tao Chen<sup>1,5</sup>

<sup>1</sup>Center for Neuron and Disease, Frontier Institute of Science and Technology, Xi'an Jiaotong University, Xi'an 710049, People's Republic of China,

<sup>2</sup>Institute for Anatomy and Cell Biology, Heidelberg University, 69120 Heidelberg, Germany, <sup>3</sup>Solomon H. Snyder Department of Neuroscience, The Johns Hopkins University School of Medicine, Baltimore, Maryland 21205, <sup>4</sup>Department of Physiology, Faculty of Medicine, University of Toronto, Toronto, Ontario M5S 1A8, Canada, and <sup>5</sup>Department of Anatomy and K.K. Leung Brain Research Center, Fourth Military Medical University, Xi'an 710032, People's Republic of China

Phosphorylation of AMPA receptor GluA1 plays important roles in synaptic potentiation. Most previous studies have been performed in the hippocampus, while the roles of GluA1 phosphorylation in the cortex remain unknown. Here we investigated the involvement of the phosphorylation of GluA1 in the LTP in the anterior cingulate cortex (ACC) using mice with a GluA1 knock-in mutation at the PKA phosphorylation site serine 845 (s845A) or CaMKII/PKC phosphorylation site serine 831 (s831A). The network LTP, which is constructed by multiple recordings of LTP at different locations within the ACC, was also investigated. We found that the expression of LTP and network LTP was significantly impaired in the s845A mice, but not in the s831A mice. By contrast, basal synaptic transmission and NMDA receptor-mediated responses were not affected. Furthermore, to uncover potential information under the current acquired data, a new method for reconstruction and better visualization of the signals was developed to observe the spatial localizations and dynamic temporal changes of fEPSP signals and multiple LTP responses within the ACC circuit. Our results provide strong evidence that PKA phosphorylation of the GluA1 is important for the network LTP expression in the ACC.

**Key words:** ACC; AMPA; LTP; mice; network; PKA

## Significance Statement

Previous studies have shown that PKA and PKC phosphorylation of AMPA receptor GluA1 plays critical roles in LTP in the hippocampus, while the roles of GluA1 phosphorylation in the cortex remain unknown. In the present study, by combining a 64-channel multielectrode system and a novel analysis and visualization method, we observed the accurate spatial localization and dynamic temporal changes of network fEPSP signals and LTP responses within the ACC circuit and found that PKA phosphorylation, but not PKC phosphorylation, of the GluA1 is required for LTP in the ACC.

## Introduction

AMPA receptors (AMPA receptors) play important roles in synaptic transmission and plasticity (Malinow and Malenka, 2002; Col-

lingridge et al., 2004; Anggono and Huganir, 2012). At baseline, most of the central synaptic currents are mediated by AMPARs. Potentiation of postsynaptic AMPARs by phosphorylation of the GluA1 subunit is one of the major synaptic mechanisms contributing to long-term potentiation (LTP), a key synaptic mechanism for learning and memory. In the hippocampus, phosphorylation of GluA1 at the serine 831 (s831) site is reported to increase the channel conductance of AMPARs (Kristensen et al., 2011), and

Received April 5, 2017; revised July 21, 2017; accepted July 28, 2017.

Author contributions: R.L.H., T.K., and M.Z. designed research; Q.S., H.-W.Z., X.-H.L., and T.C. performed research; R.L.H. and T.K. contributed unpublished reagents/analytic tools; Q.S., H.-W.Z., X.-H.L., M.Z., and T.C. analyzed data; Q.S., H.-W.Z., X.-H.L., M.Z., and T.C. wrote the paper.

This work is supported by the Canadian Institute for Health Research (CIHR) Michael Smith Chair in Neurosciences and Mental Health, Canada Research Chair, a CIHR Operating Grant (MOP-124807) and Project Grant (PJT-148648), Azrieli Neurodevelopmental Research Program and Brain Canada to M.Z. T.C. is supported by the National Natural Science Foundation of China (Grants 31371126 and 81671095). We thank Xiao-Qing Liu and Huiyan Ni for help with some experiments.

\*Q.S. and H.-W.Z. contributed equally to this work.

The authors declare no competing financial interests.

Correspondence should be addressed to either Min Zhuo or Tao Chen, Center for Neuron and Disease, Frontier Institute of Science and Technology, Xi'an Jiaotong University, Xi'an 710049, People's Republic of China. E-mail: min.zhuo@utoronto.ca or chtkkl@fmmu.edu.cn.

DOI:10.1523/JNEUROSCI.0925-17.2017

Copyright © 2017 the authors 0270-6474/17/378534-15\$15.00/0

PKA phosphorylation at the serine 845 (s845) site of the GluA1 contributes to AMPAR trafficking to the plasma membrane (Esteban et al., 2003; Oh et al., 2006). The s831 and s845 double-mutant mice showed significant deficits in LTP and spatial memory (Lee et al., 2003), providing strong evidence for the important roles of both s831 and s845 in the hippocampal LTP. However, the roles of phosphorylated GluA1 in the cortical LTP of adult animals remain unknown.

The anterior cingulate cortex (ACC) is an important area for pain perception and chronic pain, in which glutamatergic synaptic transmission undergoes long-term plastic changes after peripheral inflammation or nerve injury (Zhuo, 2008, 2016; Zhuo et al., 2011; Bliss et al., 2016). Previous studies have shown that phosphorylated GluA1 at the s845 site is increased in the ACC in animals with neuropathic pain (Xu et al., 2008; Chen et al., 2014a). Injury-induced cortical synaptic responses and behavioral sensitizations are significantly inhibited in GluA1 s845 but not s831 mutant mice (Zhuo, 2008; Chen et al., 2014a). However, it is unknown whether phosphorylation of GluA1 at the s845 or s831 sites of AMPARs actually contributes to LTP in the ACC.

To directly investigate the roles of phosphorylated GluA1 in ACC LTP, we used a 64-channel multielectrode (MED64) system to record the LTP and the network of LTP in the ACC in mice with an s845 or s831 knock-in mutation, in which the PKA or CaMKII/PKC phosphorylation sites in GluA1 were replaced with an alanine (Lee et al., 2000). We also developed a novel method from which we got better 2D and 3D visualization of the spatio-temporal signals using the low-resolution MED64 signals. We found that ACC LTP was largely impaired in the s845A mice but not in the s831A mice. Our results provide strong evidence that PKA phosphorylation, but not PKC phosphorylation, of the GluA1 is important for ACC LTP.

## Materials and Methods

**Animals.** Experiments were performed with adult (8–10 weeks old) male serine 831 mutants (s831A) mice and serine 845 mutants (s845A) mice (C57BL/6) background) and wild-type (WT) mice. All mice were maintained on a 12 h light/dark cycle with food and water provided *ad libitum*. All experiments protocols were approved by the Animal Care and Use Committee of University of Xi'an Jiaotong University.

**Slice preparation.** The general methods for preparing ACC slices were similar to those described previously (Liu et al., 2013b; Chen et al., 2014d). Adult male mice were anesthetized with ether, and the whole brain was quickly removed from the skull and submerged in ice-cold oxygenated (95% O<sub>2</sub> and 5% CO<sub>2</sub>) artificial CSF (ACSF) containing the following (in mM): 124 NaCl, 4.4 KCl, 2 CaCl<sub>2</sub>, 1 MgSO<sub>4</sub>, 25 NaHCO<sub>3</sub>, 1 NaH<sub>2</sub>PO<sub>4</sub>, and 10 glucose, pH 7.35–7.45. After cooling in the ACSF for a short time, the whole brain was trimmed to yield an appropriate sample to glue onto the ice-cold stage of a vibrating tissue slicer (VT1200S, Leica). Coronal brain slices (300 μm), containing the ACC, were prepared after the corpus callosum connection. After cutting, slices were then incubated in a submerged recovery chamber with the ACSF, for at least 2 h at room temperature.

**Preparation of the multielectrode array.** A commercial MED64 recording system (Panasonic) was used for extracellular field potential recordings. The procedure for preparation of the MED64 probe (P515A, Panasonic) used standard methods (Kang et al., 2012; Liu et al., 2013a). The MED64 probe has an array of 64 planar microelectrodes, each arranged in an 8 × 8 pattern, with an interelectrode distance of 150 μm. Before use, the surface of the MED64 probe was treated with 0.1% polyethyleneimine (P-3143, Sigma-Aldrich) in 25 mmol/L borate buffer, pH 8.4, overnight at room temperature. Before using it in the experiments, the probe surface was rinsed at least three times with sterile distilled water.

**Field potential recording in adult ACC slices.** After incubation, one slice containing the ACC was transferred to the prepared MED64 probe and perfused with the oxygenated fresh ACSF at room temperature and

maintained at a flow rate of 2 ml/min. The slice was positioned on the MED64 probe in such a way that the different layers of the ACC were entirely covered by the whole array of the electrodes, then a fine-mesh anchor was placed on the slice to ensure its stabilization during the experiments. After at least a 1 h recovery period for the slices in the recording chamber, biphasic constant-current pulse stimulation (0.2 ms) was applied to the stimulation channel to evoke the field EPSPs (fEPSPs) in the channels closest to the stimulation site. Stable baseline responses were recorded for at least 1 h, then a theta-burst stimulation (TBS; five trains of bursts with four pulses at 100 Hz, at 200 ms intervals, repeated five times at intervals of 10 s) protocol was given to induce the LTP (Chen et al., 2014d).

**Whole-cell patch-clamp electrophysiology.** Experimental procedures were based on those described previously (Zhao et al., 2005; Xu et al., 2008). Slices were transferred to a submerged recovery chamber with oxygenated ACSF at 28–30°C. After a 1 h recovery period, slices were transferred in a recording chamber on the stage of a BX51W1 microscope (Olympus) equipped with infrared differential interference contrast optics for visualized recording. The EPSCs were recorded from neurons in superficial layers (II/III) with an Axon 200B amplifier (Molecular Devices). The stimulations were delivered using a bipolar tungsten stimulating electrode placed in a deep layer (V/VI) of ACC. In the voltage-clamp configuration, recording pipettes (3–5 MΩ) were filled with the following solution (in mM): 112 Cs-Gluconate, 5 TEA-Cl, 3.7 NaCl, 0.2 EGTA, 10 HEPES, 2 MgATP, 0.3 Na<sub>3</sub>GTP, 5 QX-314, and 0.1 spermine, adjusted to pH 7.2 with CsOH, and osmolarity of 290 mOsmol. AMPA receptor-mediated EPSCs were induced by repetitive stimulations at 0.05 Hz, and neurons were voltage clamped at –60 mV in the presence of D-AP5 (50 μM). NMDA receptor (NMDAR)-mediated EPSCs were recorded at –20 mV by bathing with CNQX (20 μM). Picrotoxin (100 μM) was always present to block GABA<sub>A</sub> receptor-mediated inhibitory synaptic currents in all experiments. Data were collected and analyzed with Clampex version 10.3 and Clampfit version 10.2 software (Molecular Devices).

**Drugs.** The chemicals used in this study were as follows: picrotoxin and CNQX were purchased from Sigma-Aldrich. D-AP5 was purchased from Tocris Cookson. Drugs were prepared as stock solutions for frozen aliquots at –20°C. All these drugs were diluted from the stock solutions to the final desired concentration in ACSF before use.

**A novel method for accurate localization of multiple fEPSP peaks and network LTP.** To achieve smoother and more stable interpolation of the data acquired using the MED64 hardware with an 8 × 8 value in a 2D grid-distributed array, we developed novel software for quantitative analysis and meaningful visualization based on the combination nonlinear cubic spline interpolation method.

In this method, the low-resolution 64 array 2D signals (8 × 8 pixels) are interpolated into a high-density 2D fEPSP signal image (e.g., 640 × 640 pixels, 1280 × 1280 pixels). We use a spline interpolation method where the interpolant can be a defined type of piecewise polynomial. In numerical analysis, a spline is a term for elastic rulers for interpolating a number of predefined points. The mathematical model of the spline is the shape of such elastic rulers fixed by  $n + 1$  knots  $\{(x_i, y_i); i = 0, 1, \dots, n\}$ . It is used to interpolate between all the pairs of knots. The curvature of a curve of interpolation can be achieved using polynomials of degree 3 or higher. Here, we first apply an interpolation using polynomials of degree 3 (i.e., the case of a nonlinear cubic spline). The goal of cubic spline interpolation is to get an interpolation formula that is smooth in the first derivative and continuous in the second derivative, both within an interval and at its boundaries. The cubic spline is more stable than polynomial interpolation due to its continuous property through the second derivative without overinterpretation effects.

The workflow of the software prototype included three processing steps (see Fig. 7). The first step was to import the originally recorded MED64 values of fEPSP slopes into a 2D fEPSP value matrix including active channels and nonactive channels. Then we reconstructed a high-density 2D signals by using a nonlinear cubic spline interpolation algorithm. The advantage of this algorithm is in using higher-order cubic interpolation for keeping the accuracy and smoothness of the signals. The high-density array (from 2D array 8 × 8 pixels to 640 × 640 pixels) showed more smoothing patterns of 2D signals and continuities than the

original MED64 2D grid array at all acquisition times. In this way, we could estimate and visualize the accurate locations of multiple fEPSP signal peaks and nadirs by using contour lines. The peaks of fEPSP signals can be considered as the nodes or vertices in a graph network. The distributions of contour lines of multiple peaks of fEPSP signals show the underlying relationships among them in 2D spaces. Finally, we transferred the single 2D image into a 3D surface image by converting the strength of the fEPSP slopes into different peak values. The strength of the fEPSP slopes was digitized using a color scale bar.

**Experimental design and statistical analysis.** Experiments were performed with adult (8–10 weeks old) male s831A, s845A, and the WT mice. We used the whole-cell patch clamp to test whether the basal synaptic transmission within the ACC was affected by the GluA1 phosphorylation site mutation. The 22 neurons and 8 slices from five s845A mice, 17 neurons and 6 slices from six s831A mice, and 21 neurons and 7 slices from seven WT mice were used to record the paired-pulse facilitation (PPF). The spontaneous EPSCs (sEPSCs) were recorded in 24 neurons and 8 slices from six s845A mice, 25 neurons and 9 slices from six s831A mice, and 24 neurons and 7 slices from six WT mice. For the AMPAR-mediated input–output response, data were recorded from 20 neurons and 7 slices from six s845A mice, 23 neurons and 7 slices from six s831A mice, and 17 neurons and 6 slices from seven WT mice. For the AMPAR-mediated current–voltage relationship ( $I$ – $V$ ) response, data were recorded from 22 neurons and 9 slices from six s845A mice, 20 neurons and 7 slices from six s831A mice, and 18 neurons and 6 slices from six WT mice. For the NMDAR-mediated input–output response, data were recorded from 20 neurons and 8 slices from seven s845A mice, 19 neurons and 6 slices from seven s831A mice, and 20 neurons and 7 slices from seven WT mice. The 21 neurons and 9 slices from s845A mice, 18 neurons and 7 slices from seven s831A mice, and 23 neurons and 10 slices from seven WT mice were collected to test with Clampex version 10.3 and Clampfit version 10.2 software (Molecular Devices). In the MED64 system, 15 slices from 13 s845A mice, 15 slices from 13 s831A mice, and 15 slices from 11 WT mice were used to test the NMDAR-mediated  $I$ – $V$  response. The rise times and decay times of NMDARs were recorded from 10 neurons and 7 slices from six s845A mice, 9 neurons and 6 slices from six s831A mice, and 8 neurons and 6 slices from six WT mice. The whole-cell patch-clamp data were collected with Clampex version 10.3 and Clampfit version 10.2 software (Molecular Devices).

In the MED64 system, 15 slices from 13 s845A mice, 15 slices from 13 s831A mice, and 15 slices from 11 WT mice were used to test the LTP in ACC by TBS. Mobius software was used for all multichannel electrophysiological data acquisition and analysis. The percentages of the fEPSP slopes were normalized by the averaged value of the baseline. A new method for reconstruction and better visualization of the signals was developed to observe the spatial localizations and dynamic temporal changes of fEPSP signals and multiple LTP responses within the ACC circuit. All MED64 data were analyzed using the new method.

Results are expressed as the mean  $\pm$  SEM. The Student's  $t$  test, one-way ANOVA, and two-way ANOVA were used for statistical comparisons. The level of significance was set at  $p < 0.05$ .

## Results

### s845 mutation of the GluA1 impaired ACC LTP

To investigate the role of the s845 site of GluA1 in ACC LTP, we recorded LTP using the multichannel signals through the MED64 system (Fig. 1A). After 1 h of stable baseline recording, TBS was applied to induce network late phase of LTP (L-LTP). Unlike in wild-type mice (Fig. 1F–J), TBS failed to induce L-LTP of the fEPSP slope in most of the active channels in the s845A mice. As shown in a typical sample slice with 19 active responses in the s845A mice (Fig. 1A–E), only two active channels showed L-LTP ( $168.1 \pm 20.3\%$  of baseline) lasting for 4 h and five active channels showed a short-term LTP (S-LTP) lasting  $< 3$  h, while most of the channels (12 channels) showed no potentiation throughout the entire recording period. The final averaged slope of all 19 channels was  $101.0 \pm 6.0\%$  of the baseline at 4 h after TBS induc-

tion (Fig. 1E). In a total of 264 active channels from 15 slices from 13 mice, TBS induced L-LTP in 67 channels (25.4%;  $141.9 \pm 4.0\%$  of the baseline), S-LTP in 48 channels (18.2%), but no LTP in 149 channels (56.4%). In a sum of the 264 channels, TBS failed to induce L-LTP ( $108.3 \pm 4.8\%$  of the baseline;  $t_{(14)} = -1.795$ ,  $p = 0.0943$ , paired  $t$  test; see Fig. 4F).

In the ACC of WT mice, however, TBS induced L-LTP in most of the active channels, which was similar to our previous reports (Chen et al., 2014b; Song et al., 2015). As shown in one typical sample slice with 21 active channels (Fig. 1F–I), 15 channels showed L-LTP ( $157.7 \pm 6.2\%$  of the baseline), 3 channels showed S-LTP, and 3 channels showed no potentiation. The final averaged slope of 21 channels was  $141.4 \pm 5.2\%$  of the baseline at 4 h after TBS induction (Fig. 1J). In a total of 15 slices from 11 mice, we found that TBS induced L-LTP in 83.8% (233 from 278 active channels) of active channels and their averaged fEPSP slope reached to  $158.8 \pm 2.5\%$  of the baseline. In the other 45 channels, 18 channels (6.5%) showed S-LTP, and 27 channels (9.7%) showed no potentiation. The fEPSP slope of the total 278 channels was potentiated to  $149.7 \pm 3.2\%$  of the baseline at 4 h after TBS ( $t_{(14)} = -17.868$ ,  $p = 4.928E-11$ , paired  $t$  test), and that was significantly greater than that in s845A mice ( $t_{(28)} = 7.656$ ,  $p = 2.44E-8$ , unpaired  $t$  test; see Fig. 4F). It was also indicated that the number of channels showing L-LTP was affected (see Fig. 4G), as follows: s845A mice showed significantly fewer channels with L-LTP (WT mice,  $15.53 \pm 1.75$  channels; s845A mice,  $4.47 \pm 1.87$  channels;  $t_{(28)} = 5.199$ ,  $p = 1.61E-5$ , unpaired  $t$  test), more channels with no LTP (WT mice,  $1.80 \pm 0.41$  channels; s845A mice,  $9.93 \pm 1.80$  channels;  $t_{(28)} = -6.456$ ,  $p = 5.42E-7$ , unpaired  $t$  test), and more channels with S-LTP (WT mice,  $1.20 \pm 0.47$  channels; s845A mice,  $3.20 \pm 0.92$  channels;  $t_{(28)} = -2.36$ ,  $p = 0.0255$ , unpaired  $t$  test;  $n = 15$  slices from 11 WT mice and 15 slices from 13 s845A mice; see Fig. 4H).

### AMPA-mediated synaptic transmission was not changed in s845A mice

Next, we explored whether or not the basal synaptic transmission within the ACC was affected by the GluA1 phosphorylation site mutation. By using whole-cell patch-clamp method, we recorded neurons in the superficial layers (II/III) by stimulating the deep layers (V/VI) of the ACC (Fig. 2A). PPF and sEPSC, the two simple measurements for measuring the presynaptic transmitter release possibility and postsynaptic receptor efficiency, were tested first. We examined the PPF at different stimulus intervals of 35, 50, 75, 100, and 150 ms and found that the PPF ratios were not different between the WT and s845A mice ( $F_{(1,214)} = 0.243$ ,  $p = 0.913$ , two-way ANOVA;  $n = 21$  neurons and 7 slices from WT mice and 22 neurons and 8 slices from s845A mice; Fig. 2B). Consistently, neither the frequency (WT mice,  $3.0 \pm 0.6$  Hz; s845A mice,  $2.8 \pm 0.3$  Hz;  $t_{(46)} = 0.345$ ,  $p = 0.732$ ) nor the amplitude (WT mice,  $9.8 \pm 0.4$  pA; s845A mice,  $10.2 \pm 0.5$  pA;  $t_{(46)} = -0.573$ ,  $p = 0.596$ ) of the sEPSCs was changed between WT and s845A mice ( $n = 24$  neurons and 7 slices from WT mice and 24 neurons and 8 slices from s845A mice; unpaired  $t$  test; Fig. 2C–E).

We then tested the input (stimulation intensity)–output (EPSC amplitude) efficiency and  $I$ – $V$  relationship of the AMPAR-mediated synaptic responses. The slopes of the AMPAR-mediated input–output curve were not different in WT and s845 mice ( $F_{(1,234)} = 0.057$ ,  $p = 1.000$ , two-way ANOVA;  $n = 17$  neurons and 6 slices from WT mice and 20 neurons and 6 slices from s845A mice; Fig. 2F). The same tendency was also found in the  $I$ – $V$  curve ( $F_{(1,359)} = 1.424$ ,  $p = 0.485$ , two-way ANOVA;  $n = 18$  neurons and 6 slices

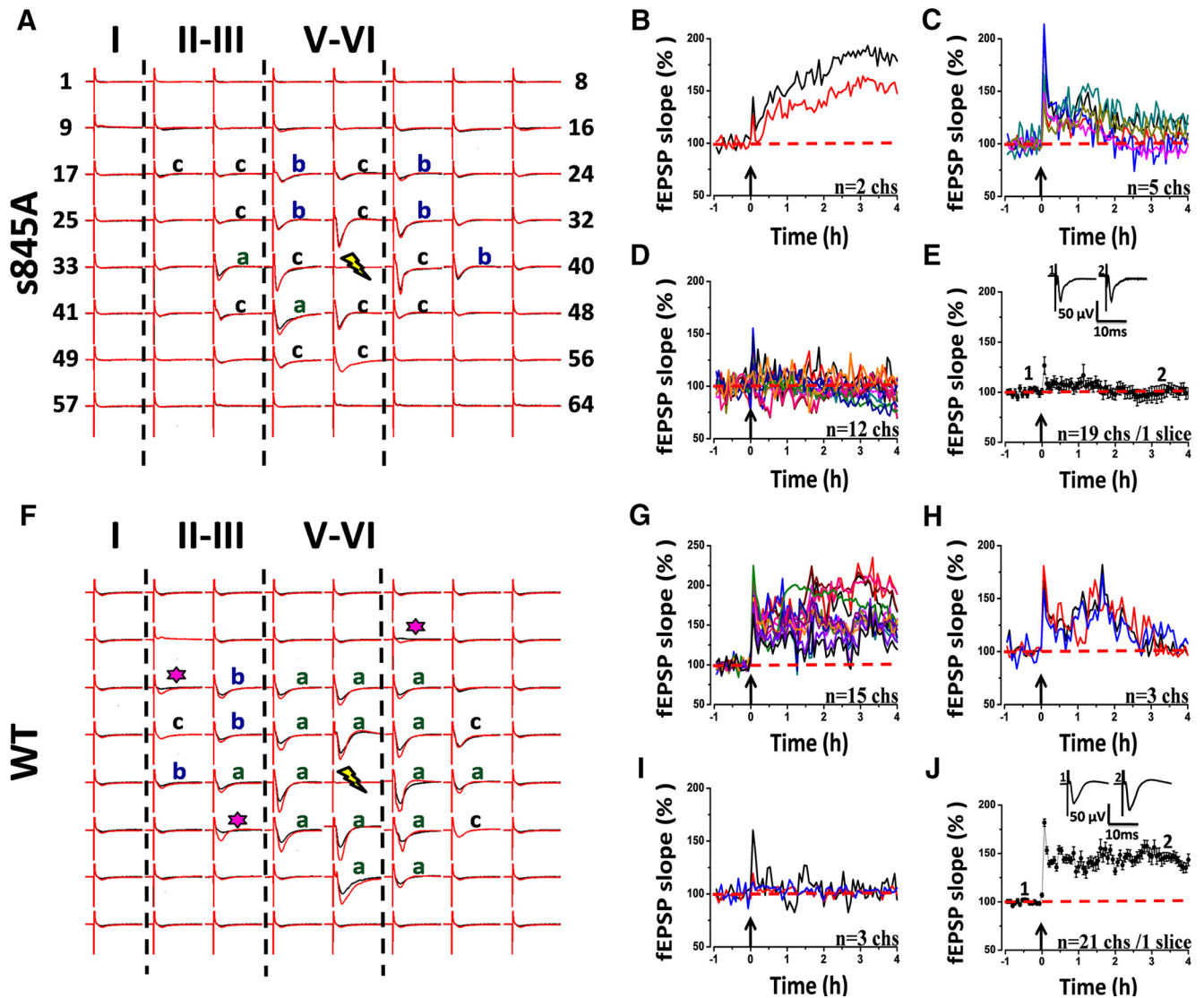


**Figure 1.** s845 mutation of the GluA1 impaired the LTP. **A, F**, Two mapped samples show the network fEPSP in the ACC of s845A mice (**A**) and WT mice (**F**). The fEPSPs were induced by electrical stimulation on one channel (37, marked as light yellow) and were recorded from the other 63 channels 1 h before (black) and 4 h after (red) TBS. Asterisks indicated the channels with recruited fEPSPs in the ACC of WT mice. Superimposed sample traces at different time points (1 h before and 4 h after TBS) showed the following three types of plasticity: channels showing L-LTP (**a**), channels showing S-LTP (**b**), and channels without potentiation (**c**). **B–D**, The temporal changes of the fEPSP slopes with three types of plasticity from one slice from the s845A mouse: 2 channels with L-LTP (**B**), 5 channels with S-LTP (**C**), and 12 channels without potentiation (**D**). The final averaged slope for all 19 active channels at 4 h after TBS ( $101.0 \pm 6.0\%$  of the baseline) in the slice from the s845A mouse was shown in **E**. **G–I**, The temporal changes of the fEPSP slopes from one slice from the WT mouse: 15 channels with L-LTP (**G**), 3 channels with short-term potentiation (**H**), and 3 channels without potentiation (**I**). The final averaged slope for all 21 active channels at 4 h after TBS ( $141.4 \pm 5.2\%$  of the baseline) in the WT slice was shown in **J**. Arrows in **B–E** and **G–J** indicate the starting point of TBS application.

from WT mice and 22 neurons and 9 slices from s845A mice; Fig. 2G). These results suggest that the AMPAR-mediated basal excitatory synaptic transmissions were not different between the WT and s845A mice.

#### NMDA receptor-mediated responses in s845A mice

NMDARs play crucial roles in the induction of LTP in the ACC (Zhao et al., 2005; Zhuo, 2008; Bliss et al., 2016). We next checked whether the properties of NMDAR-mediated responses were affected in s845A mice. We found that the NMDAR-mediated input–output curves were not different between the WT and s845A mice ( $F_{(1,199)} = 0.0146$ ,  $p = 1.000$ , two-way ANOVA;  $n = 20$  neurons and 7 slices from WT mice and 20 neurons and 8 slices from s845A mice; Fig. 3A). Similarly, the NMDAR-mediated  $I-V$  curve was not changed in the s845A mice ( $F_{(1,395)} = 0.411$ ,

$p = 0.914$ , two-way ANOVA;  $n = 23$  neurons and 10 slices from WT mice and 21 neurons and 9 slices from s845A mice; Fig. 3B). In consistent with this, the rise time and decay time of the NMDAR-mediated EPSCs were not changed (rise time:  $15.4 \pm 1.3$  ms in WT mice;  $14.8 \pm 1.2$  ms in s845A mice;  $t_{(16)} = 0.342$ ,  $p = 0.737$ ; decay time:  $213.3 \pm 16.5$  ms in WT mice;  $229.8 \pm 11.4$  ms in s845A mice;  $t_{(16)} = -0.899$ ,  $p = 0.382$ , unpaired  $t$  test;  $n = 8$  neurons and 6 slices from WT mice and 10 neurons and 7 slices from s845A mice; Fig. 3C). These results suggest that the properties of NMDARs in ACC neurons were not different between WT and s845A mice.

#### s831 mutation of the GluA1 did not affect the LTP

Since CaMKII- and PKC-dependent phosphorylation of GluA1 play important roles for LTP expression in the hippocampus (Lee

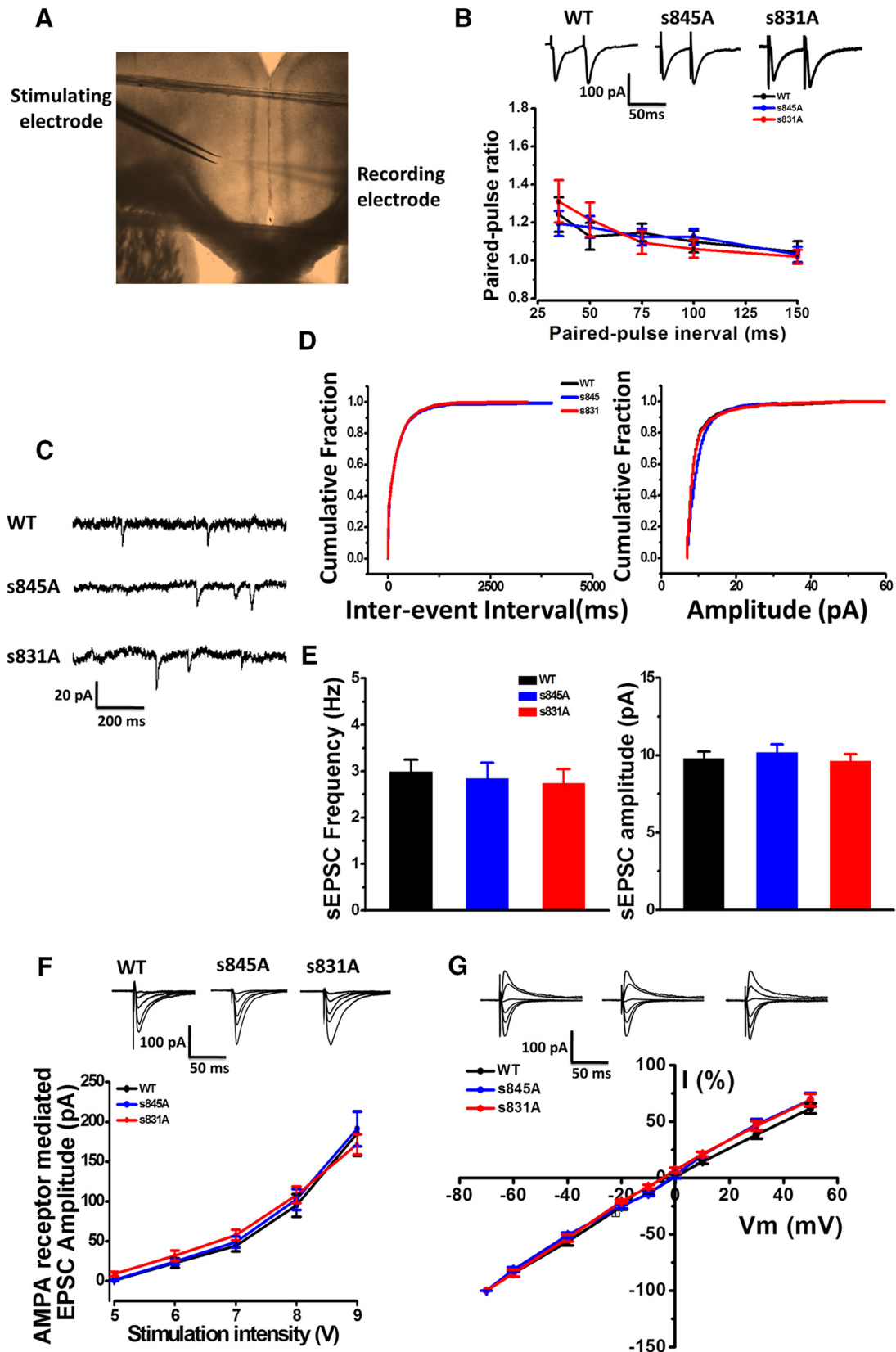


**Figure 2.** Both s845 and s831 mutations of the GluA1 did not change the AMPA receptor-mediated basal synaptic transmission. **A**, Schematic diagram showed the location of the stimulation electrode in the layer V/VI and recording electrode for one pyramidal neuron in layer II/III of the ACC. **B**, Sample traces and summarized results showed the paired-pulse ratio recorded with intervals of 35, 50, 75, 100, and 150 ms in WT, s845A, and s831A mice. **C**, Representative mEPSC recorded in the ACC neuron from WT and mutant mice. **D**, Cumulative histograms of the interevent interval (left) and amplitude (right) of mEPSCs from sample neurons of WT and mutant mice. **E**, Summarized results of the frequency (left) and amplitude (right) of sEPSCs. **F**, **G**, Synaptic input–output curves (**F**) and *I*–*V* curves (**G**) of AMPAR-mediated evoked EPSCs in WT, s845A, and s831A mice.

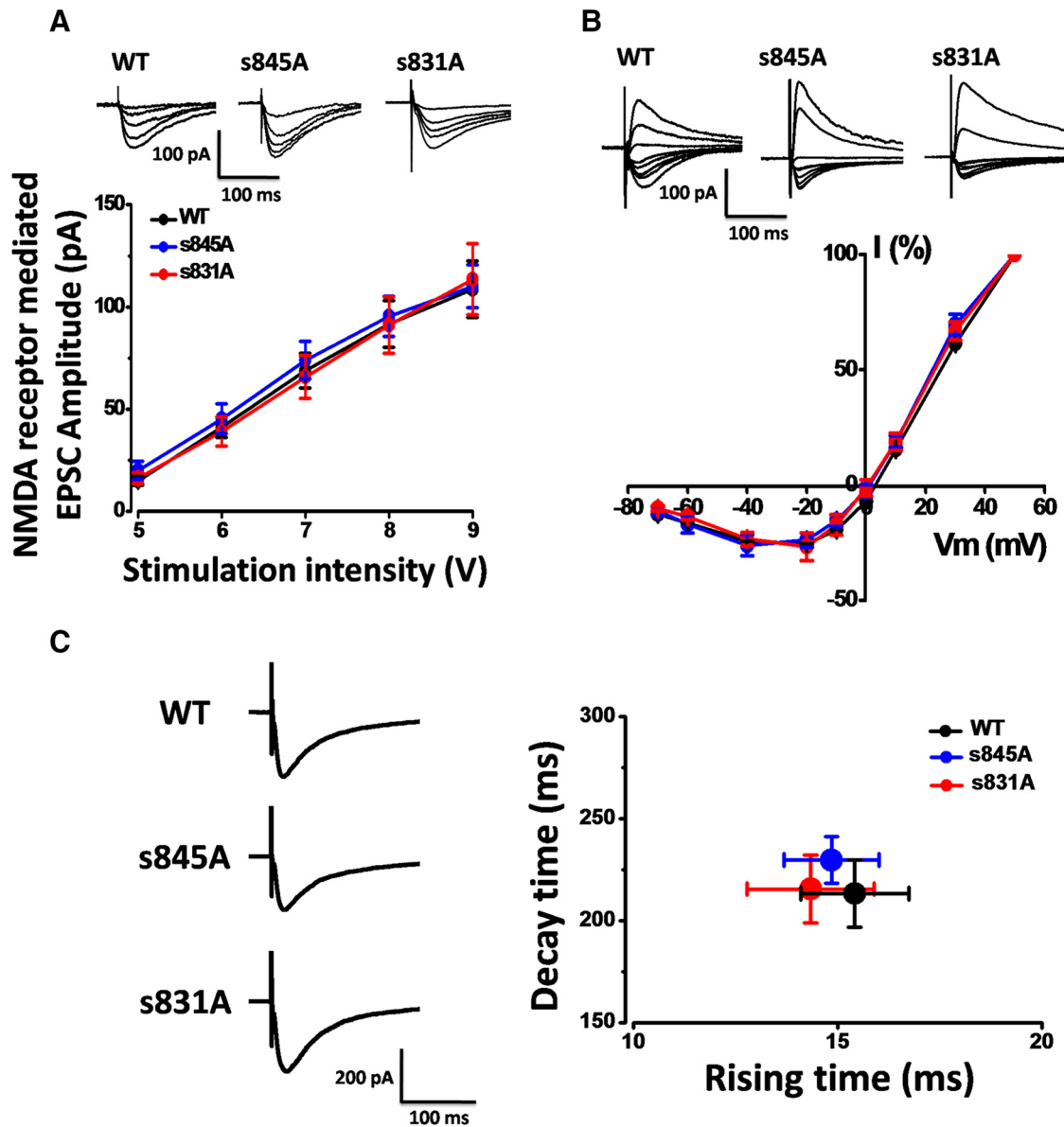


**Figure 3.** NMDA receptor-mediated responses were not changed in either s845A or s831A mice. *A*, Synaptic input–output curves of NMDA receptors mediated evoked EPSCs in WT, s845A, and s831A mice. *B*, Synaptic *I*–*V* curves of NMDA receptors mediated evoked EPSCs in WT, s845A, and s831A mice. *C*, Normalized traces (left) and pooled data of rise time and decay time (right) in WT, s845A, and s831A mice.

et al., 2000), we then applied TBS to determine whether LTP is also impaired in the ACC of s831A mice. We found that LTP was induced in most of the active channels in the s831A mice, with a similar pattern in WT mice. As shown in a typical sample slice with 18 active responses (Fig. 4*A*), 12 channels showed L-LTP ( $150.4 \pm 8.8\%$  of baseline), 3 channels showed S-LTP, and 3 channels showed no LTP (Fig. 4*B–D*). The final averaged slope of all 18 channels was  $133.6 \pm 8.3\%$  of the baseline at 4 h after TBS induction (Fig. 4*E*). In a total of 15 slices from 13 mice, we found that 77.3% (211 from 273 channels) of active channels showed L-LTP ( $156.1 \pm 2.8\%$  of the baseline), 30 channels (11.0%) showed S-LTP, and 32 channels (11.7%) showed no potentiation. The fEPSP slope of all 273 channels was potentiated to  $146.0 \pm 3.9\%$  of the baseline, which was not different with the WT mice ( $t_{(28)} = -0.726, p = 0.474$ , unpaired *t* test; Fig. 4*F*). Further analysis showed that the occurrence of L-LTP and S-LTP and no LTP of s831A mice was not different with WT mice (L-LTP:  $t_{(28)} =$

$0.783, p = 0.440$ ; S-LTP:  $t_{(28)} = -0.8, p = 0.336$ ; no LTP:  $t_{(28)} = -0.333, p = 0.563$ , unpaired *t* test) but significantly different with s845A mice (L-LTP:  $t_{(28)} = 6.268, p = 8.93E-7$ ; no LTP:  $t_{(28)} = -6.16, p = 1.19E-7$ ; S-LTP:  $t_{(28)} = -1.21, p = 0.236$ , unpaired *t* test; Fig. 4*H*). These findings suggest that the s831 mutation of GluA1 has no important impact on LTP expression in the ACC.

The basal synaptic transmission in the ACC of s831A mice was also tested. These experiments demonstrated that the PPF ( $F_{(1,189)} = 0.973, p = 0.325$ , two-way ANOVA;  $n = 17$  neurons and 6 slices from s831A mice and 21 neurons and 7 slices from WT mice;  $F_{(1,194)} = 0.900, p = 0.465$ , two-way ANOVA;  $n = 17$  neurons and 6 slices from s831 mice and 22 neurons and 8 slices from s845A mice), sEPSC (frequency: s831A mice,  $2.7 \pm 0.3$  Hz; s831A vs WT mice:  $t_{(47)} = -0.626, p = 0.534$ ; s831A vs s845A mice,  $t_{(47)} = -0.221, p = 0.826$ , unpaired *t* test; amplitude: s831A mice,  $9.6 \pm 0.5$  pA; s831A vs WT mice,  $t_{(47)} = 0.29, p = 0.773$ ; s831A vs s845A mice,  $t_{(47)} = 0.822, p = 0.415$ , unpaired *t* test;  $n = 25$

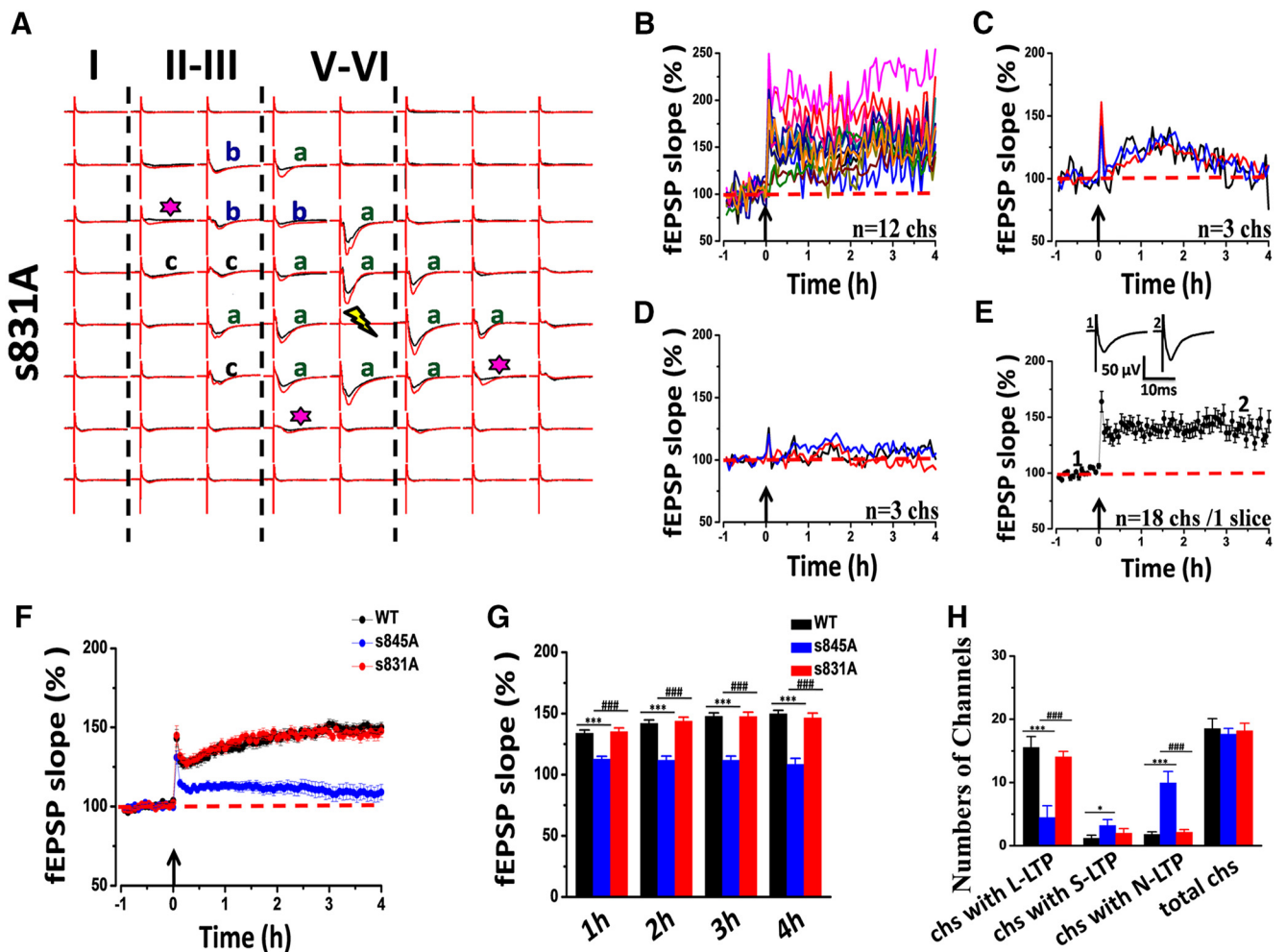


**Figure 4.** Network plasticity of the fEPSP in the ACC of s831A mice. **A**, One samples showed the network fEPSP in the ACC of s831A mice. **B–D**, The temporal changes of fEPSP slopes from one slice from the s831A mouse: 12 channels with L-LTP (**B**), 3 channels with short-term potentiation (**C**), and 3 channels without potentiation (**D**). **E**, The final averaged slope for all 18 active channels at 4 h after TBS ( $133.6 \pm 8.3\%$  of the baseline) in the s831A slice was shown. **F**, The averaged fEPSP slopes of all recorded channels in WT (15 slices/11 mice), s845A and s831A mice (both from 15 slices/13 mice). **G**, The averaged fEPSP slopes from total active channels of WT, s845A, and s831A mice at different time points after the TBS. **H**, The average number of the channels showed three types of plasticity from WT, s845A, and s831A mice. Arrows in **B–F** indicate the starting point of TBS application. \* $p < 0.05$ , \*\*\* $p < 0.001$ , WT mice vs s845A mice. ### $p < 0.001$ , s845A mice vs s831A mice.

neurons and 9 slices from s831A mice, 24 neurons and 7 slices from WT mice, and 24 neurons and 8 slices from s845A mice), the AMPAR-mediated synaptic response (input–output curve: s831A vs WT mice,  $F_{(1,199)} = 1.045$ ,  $p = 0.401$ ; s831A vs s845A mice,  $F_{(1,214)} = 1.243$ ,  $p = 0.281$ , two-way ANOVA;  $n = 23$  neurons and 7 slices from s831A mice, 17 neurons and 6 slices from WT mice, and 20 neurons and 6 slices from s845A mice;  $I-V$  curve: s831A vs WT mice,  $F_{(1,341)} = 1.009$ ,  $p = 0.429$ ; s831A vs s845A mice,  $F_{(1,377)} = 0.634$ ,  $p = 0.749$ , two-way ANOVA;  $n = 20$  neurons and 7 slices from s831A mice, 18 neurons and 6 slices from WT mice, and 22 neurons and 9 slices from s845A mice), and NMDAR-mediated synaptic responses (input–output curve: s831A vs WT mice,  $F_{(1,194)} = 0.0639$ ,  $p = 0.992$ ; s831A vs s845A mice,  $F_{(1,194)} = 0.129$ ,  $p = 0.972$ , two-way ANOVA;  $n = 19$  neurons and 6 slices from s831A mice, 20 neurons and 7 slices from WT mice, and 20 neurons and 8 slices from s845A mice;  $I-V$  curve: s831A vs WT mice,  $F_{(1,368)} = 0.387$ ,  $p = 0.927$ ; s831A vs s845A mice,  $F_{(1,350)} = 0.118$ ,  $p = 0.999$ , two-way ANOVA;  $n = 18$  neurons and 7 slices from s831A mice, 23 neurons and 10 slices from WT mice, and 21 neurons and 9 slices from s845A mice; rise time,  $14.3 \pm 1.6$  ms in s831A mice; s831A vs WT mice,  $t_{(15)} = 0.342$ ,  $p = 0.737$ ; s831A vs s845A mice,  $t_{(17)} = -0.279$ ,  $p = 0.783$ ;

decay time,  $215.5 \pm 16.5$  ms in s831A mice; s831A vs WT mice,  $t_{(15)} = -0.1$ ,  $p = 0.921$ ; s831A vs s845A mice,  $t_{(17)} = -0.765$ ,  $p = 0.455$ , unpaired  $t$  test;  $n = 9$  neurons and 6 mice from s831A mice, 8 neurons and 6 slices from WT mice, and 10 neurons and 7 slices from s845A mice) were not different in the s831A mice compared with those in the WT and s845A mice (Figs. 2, 3).

#### Recruited responses in the ACC of WT and s831A mice but not s845A mice

One of the advantages of the multichannel recording system is that we can observe the recruitment of channels, which are originally inactive but can be recruited by TBS induction (Chen et al., 2014d). In WT mice,  $18.53 \pm 1.55$  channels per slice (15 slices and 11 mice) were originally activated and showed fEPSP during the baseline recording. However,  $2.5 \pm 0.3$  channels were recruited after TBS (Fig. 5G). In consistent with our previous observation (Chen et al., 2014c), the recruited channels were located on the edge of the basal active area (Fig. 5A).

We then tested whether s845 or s831 mutations may affect the TBS-induced channel recruitment. We found that the number of basal activated channels was not changed in s845A and s831A mice, compared with WT mice (s845A mice,  $17.67 \pm 0.88$  chan-

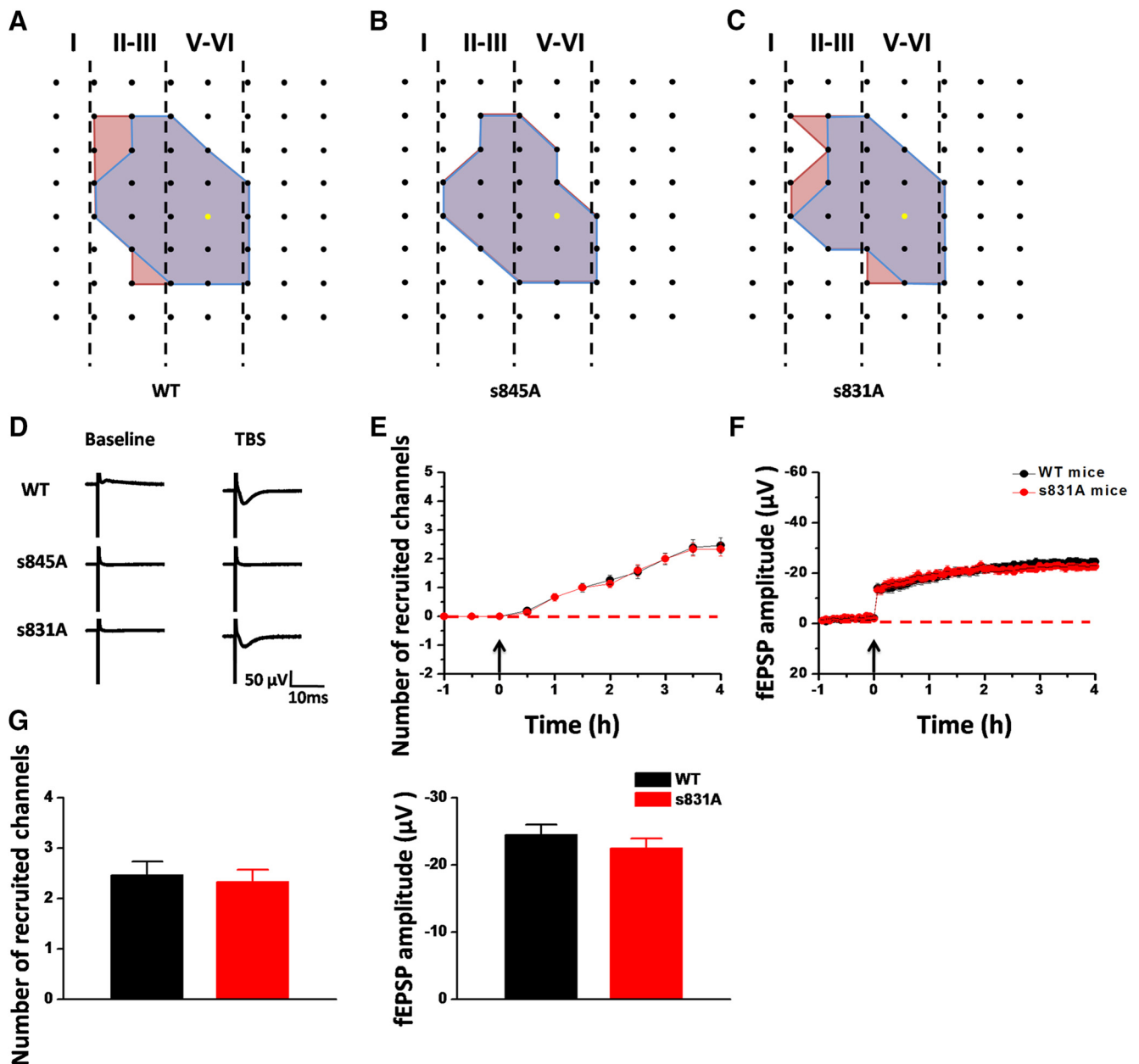


**Figure 5.** The temporal changes of recruited responses in WT, s845A, and s831A mice. **A–C**, Sample slices showed the distribution of the basal activated channels (blue) and the TBS-recruited channels (red) in WT mice (**A**) and s831 mice (**C**) but not in s845A mice (**B**). **D**, Superimposed samples showed the recruited responses induced by TBS. **E, F**, The temporal changes of the number (**E**) and amplitude (**F**) of the recruited fEPSPs in WT and s831A mice. **G**, The averaged number (left) and amplitude (right) of recruited channels in WT and s831A mice.

nels; s831A mice,  $18.2 \pm 1.17$  channels;  $n = 15$  slices and 13 s845A mice and 15 slices and 13 s831A mice;  $F_{(2,42)} = 0.223$ ,  $p = 0.801$ , one-way ANOVA). However, recruited channels were observed only in s831A mice, not in s845A mice (Fig. 5B,C).

The time courses of the changed fEPSP slope in the recruited channels were further shown in Figure 5D–F. In WT and s831A mice, the number of recruited channels gradually increased after TBS induction (Fig. 5E). In these recruited channels, TBS-induced fEPSPs were gradually potentiated, and the amplitude finally became as large as  $24.5 \pm 1.5 \mu\text{V}$  in WT mice and  $22.5 \pm 1.4 \mu\text{V}$  in s831A mice at 4 h after TBS induction (Fig. 5F). Neither the numbers of recruited channels ( $t_{(28)} = 0.386$ ,  $p = 0.702$ , unpaired  $t$  test) nor their fEPSP amplitudes ( $t_{(70)} = -1.065$ ,  $p = 0.291$ , unpaired  $t$  test) were different in WT and s831A mice (Fig. 5G).

### Spatial and temporal tracing of fEPSPs

For a better understanding of the distribution patterns of the active responses, we analyzed their spatial distribution in different layers of the ACC and their temporal changes before and after TBS in WT, s845A, and s831A mice. At first, we plotted the fEPSP slopes from all 63 recorded channels with active and nonactive (defined as 0 mV/ms) responses at 0.5 h before and 4 h after TBS ( $n = 15$  slices acquired in each group; Fig. 6A–C) into a 2D channel–slope strength system. When we stimulated the channel in a deep layer (channel 37), the active responses were observed in both the deep and superficial layers around it. The peak intensity of fEPSP slopes was near channels 27–29, the superficial layers of the stimulation site (also shown in Fig. 1A). Basal fEPSP slopes were similar in the three types of mice. However, the average level of potentiation

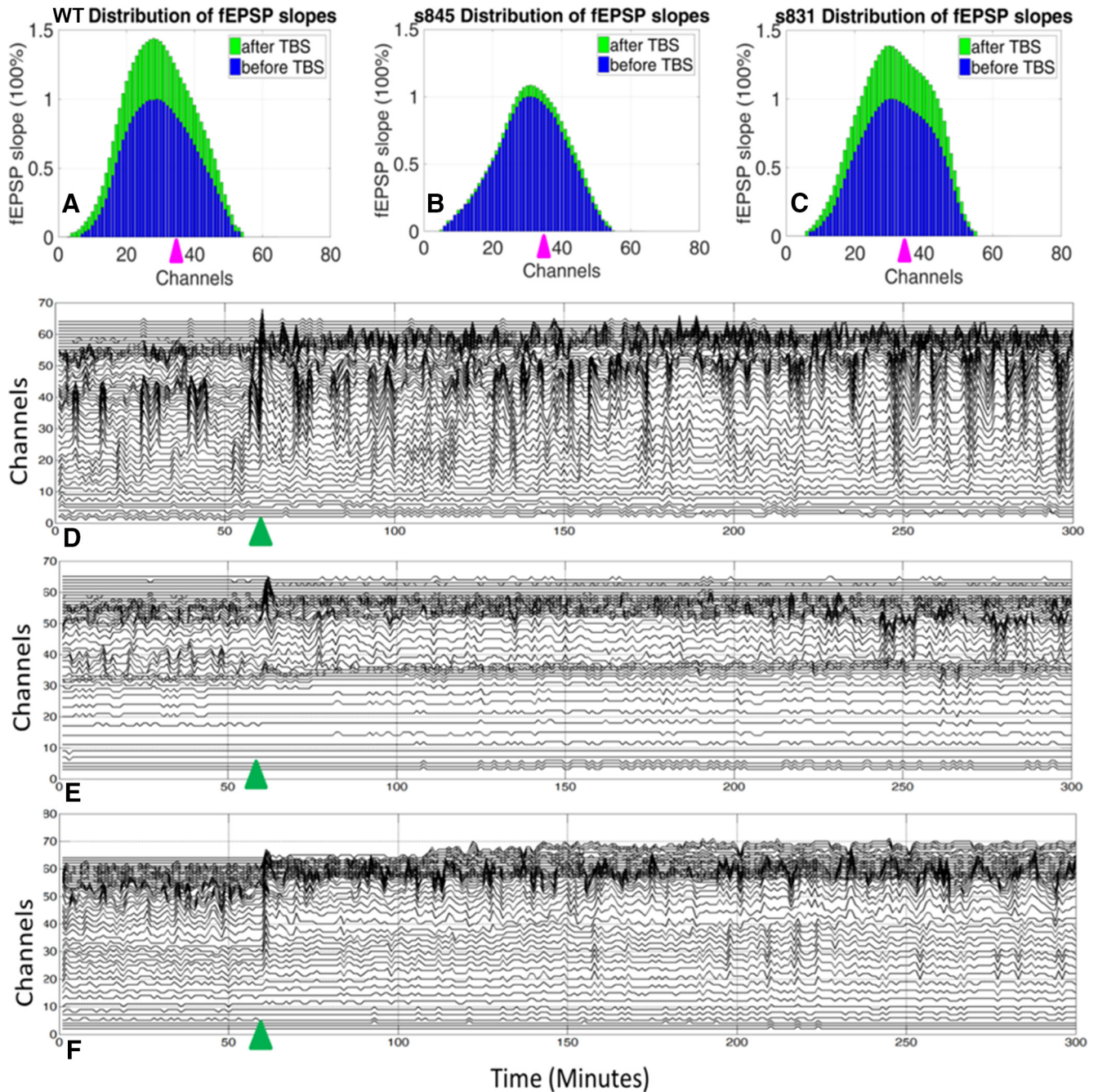


**Figure 6.** The spatiotemporal accumulated distribution of fEPSP slope for all 64 channels. **A–C**, The channel distribution of averaged fEPSP slope before and after TBS in WT (**A**), s845A (**B**), and s831A (**C**) mice. The stimulating site (channel 37) in each panel is indicated with a purple triangle. **D–F**, The average fEPSP signals from all channels in WT (**D**), s845A (**E**), and s831A mice (**F**) were recorded over time. The curves in all channels show the temporal changes of the normalized fEPSP slope and recruited responses after TBS using the mean value of all 15 measured slices. TBS application time was indicated with green triangles.

of fEPSP slopes after TBS was quite different, in which much smaller potentiation was shown in s845A (Fig. 6B) mice compared with WT (Fig. 6A) and s831A mice (Fig. 6C). We then plotted the temporal changes in each channel before and after TBS, in which the spatial distribution of responses from all 63 recording channels were plotted on the  $y$ -axis and their temporal changes were plotted on the  $x$ -axis ( $n = 15$  slices in each type of mice; Fig. 6D–F). The traces showed that TBS could induce stronger potentiation of fEPSP slopes in most of the channels in WT and s831A mice than in s845A mice.

#### Spatiotemporal pattern of LTP

To determine the accurate spatiotemporal properties of the fEPSP signals, we developed a software prototype that can reconstruct smoother and more stable interpolation of signals ( $640 \times 640$  pixels) by using a nonlinear cubic spline interpolation algorithm in an optimal way (for detailed description, see Materials and Methods). By this method, the originally recorded MED64 values of fEPSP slopes, including active channels and nonactive channels (Fig. 7A, D), were reconstructed into high-density 2D signals ( $640 \times 640$  pixels; Fig. 7B, E) and then transferred to 3D

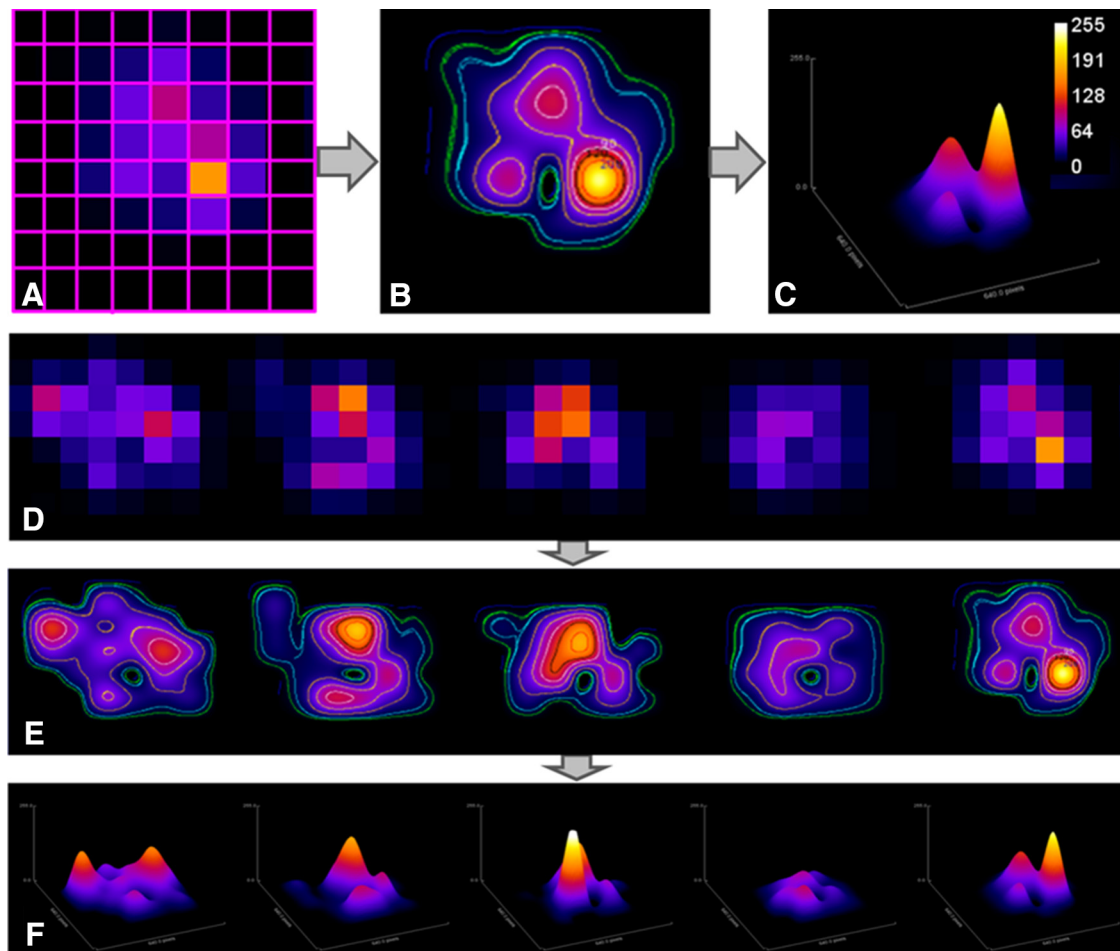


**Figure 7.** A workflow for reconstructing sparsely grid-distributed signals into highly representative spatial 2D and 3D signals. **A–C**, A workflow showed the interpolation of the signals from MED64 channels ( $8 \times 8$ ; **A**) to a  $640 \times 640$  2D image (**B**) and its 3D version (**C**). **D**, The  $8 \times 8$  pixels MED64 signals in five randomly selected slices in WT mice. **E**, The interpolated 2D image showed the continuity of signals as well as the accurate localization of fEPSP peaks with contour lines in each acquisition slice. **F**, 3D surfaces showed the peaks of fEPSP signals and their locations.

signals (Fig. 7C,F). This is helpful to show smoother patterns for 2D signals and continuities at all acquisition times.

The multiple fEPSP peaks were considered as vertices of a graph network, and the contour line map showed the spatial distribution of the LTP network. In this way, we applied the similar acquisition and reconstruction methods for analyzing data before and after TBS for all acquired datasets (Figs. 8–10). The values of the fEPSP slope in three representative slices with respect to WT, s845A, and s831A mice were shown (Fig. 8). The values of fEPSP signals at baseline (Fig. 8A,D,G), after TBS (Fig. 8B,E,H), and the differences between values at baseline and after TBS (Fig. 8C,F,I) were presented in a color-encoded 2D contour line map with strength calibration color bars, respectively.

The locations of multiple fEPSP signal peaks and the distribution of networks were accurately computed using the height levels of contour lines. The 3D surfaces (Fig. 8J–R) were reconstructed based on the 2D color map shown in Figure 8A–I, by using the height level contour lines in a 3D version with a calibration bar. From these figures, we were able to localize the spatial distribution and the strength of the basal network active responses and their potentiation effect. Based on the 2D and 3D versions of the reconstructed results (Fig. 8), the difference in network responses before and after TBS were accurately exhibited. Although the intensity and spatial distributions of the basal fEPSP slopes were similar, it is easy to find that TBS significantly

increased the intensity in most of the active areas surrounding the stimulation sites in WT and s831A mice. However, very weak potentiation was observed in the s845A mice, indicating that the s845 site of GluA1 is important for the network LTP in the ACC.

Further quantitative analyses of recruited responses were visualized in spatiotemporal 3D spaces. The TBS-induced recruitment in WT, s831A, and s845A mice could be easily measured and visualized in 3D spatiotemporal space (Fig. 9). In typical samples of WT, s845A, and s831A mice, the spatial characteristics of the network active responses were presented along the time course to show their temporal changes during the whole experimental procedure (Fig. 9A,D,G) or during split procedures [at baseline (Fig. 9B,E,H) and after TBS phases (Fig. 9C,F,I), respectively]. We found that the recruited responses, which were located on the edges of the active areas, emerged after TBS induction and increased gradually in WT mice (Fig. 9A–C) and s831A mice (Fig. 9G–I), but not in s845A mice (Fig. 9D–F).

#### Spatiotemporal characterization of the network L-LTP

We computed the spatial strength distribution of L-LTP (Fig. 10A–I, yellow calibration bar) and the spatial frequency distribution of L-LTP (Fig. 10J–R, blue calibration bar) in 63 recording channels (channels with S-LTP and no potentiation were not included). Based on the originally acquired low-resolution 64-

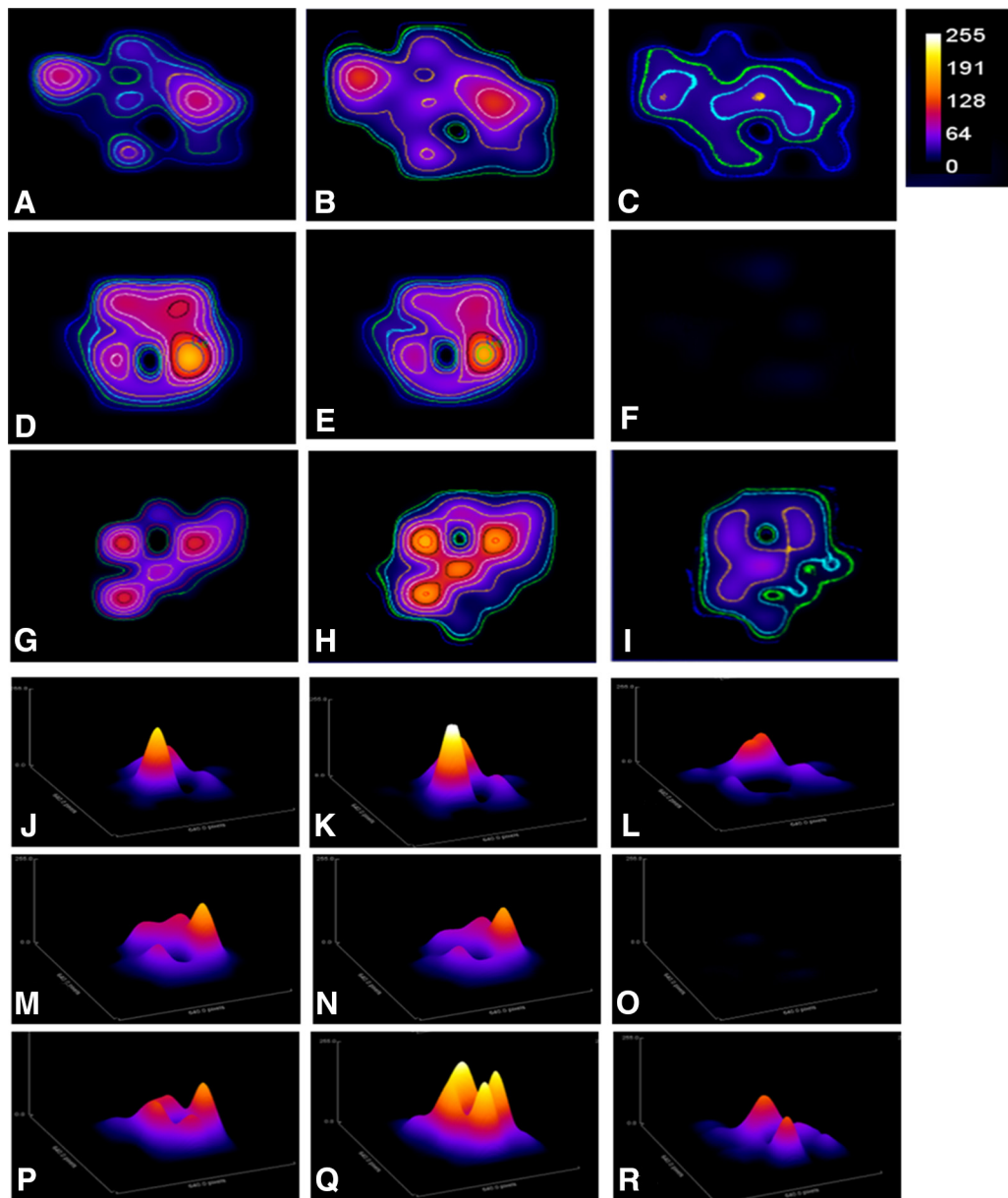


**Figure 8.** The spatial distribution pattern of LTP in three types of mice. **A–C**, The high-density images showed the value of fEPSP slopes before (**A**) and 4 h after TBS (**B**) in one sample slice of WT mice; their difference was shown in **C**. **D–F**, The value of the fEPSP slope before and after TBS in one sample slice of s845A mice (**D**, **E**); their difference was shown in **F**. **G–I**, The values of the fEPSP slope before and after TBS in one sample slice from s831A mice (**G**, **H**); their difference was shown in **I**. **J–L**, The 3D versions of **A–C** were shown respectively. **M–O**, The 3D versions of **D–F** were shown respectively. **P–R**, The 3D versions of **G–I** were shown respectively.

channel datasets with  $8 \times 8$  values, the averages of fEPSP slopes (strength) at 4 h after TBS induction were computed for WT mice (Fig. 10A), s845A mice (Fig. 10D), and s831A mice (Fig. 10G;  $n = 15$  slices in each type of mice). Then we reconstructed the 63 values from 2D signals into the high-density  $640 \times 640$  pixel 2D (Fig. 10B, E, H) and 3D representations (Fig. 10C, F, I), respectively. The probability distributions of the spatial strength network of L-LTP with multiple L-LTP peaks (vertices) were thus quantitatively and accurately visualized. Similarly, the probability distributions of the spatial frequency network of L-LTP were computed to show the spatial distributions of the L-LTP on the same measured slices, so that we could easily observe where L-LTP often happens. The probability distributions of spatial frequency L-LTP network were shown with the averaged 63 channels as the 2D map (Fig. 10J, M, P), a reconstructed highly

representative contour line map (Fig. 9K, N, Q), and a 3D surface map (Fig. 10L, O, R).

According to the quantitative analysis, we found that the spatial strength (Fig. 10C, F, I) and spatial frequency (Fig. 10L, O, R) of the network L-LTP are often formed as a ring distribution surrounding the location where stimulation was delivered. The spatial strength and spatial frequency distributions of L-LTP were similar in both WT and s831A mice, but obviously were weak in s845A mice.

## Discussion

In the present study, by using genetic mutant mice in the phosphorylation of GluA1 at s845 and s831 sites of AMPARs, we found that PKA phosphorylation site s845 of GluA1 is important for the ACC L-LTP. By using a multiple-channel MED64 field

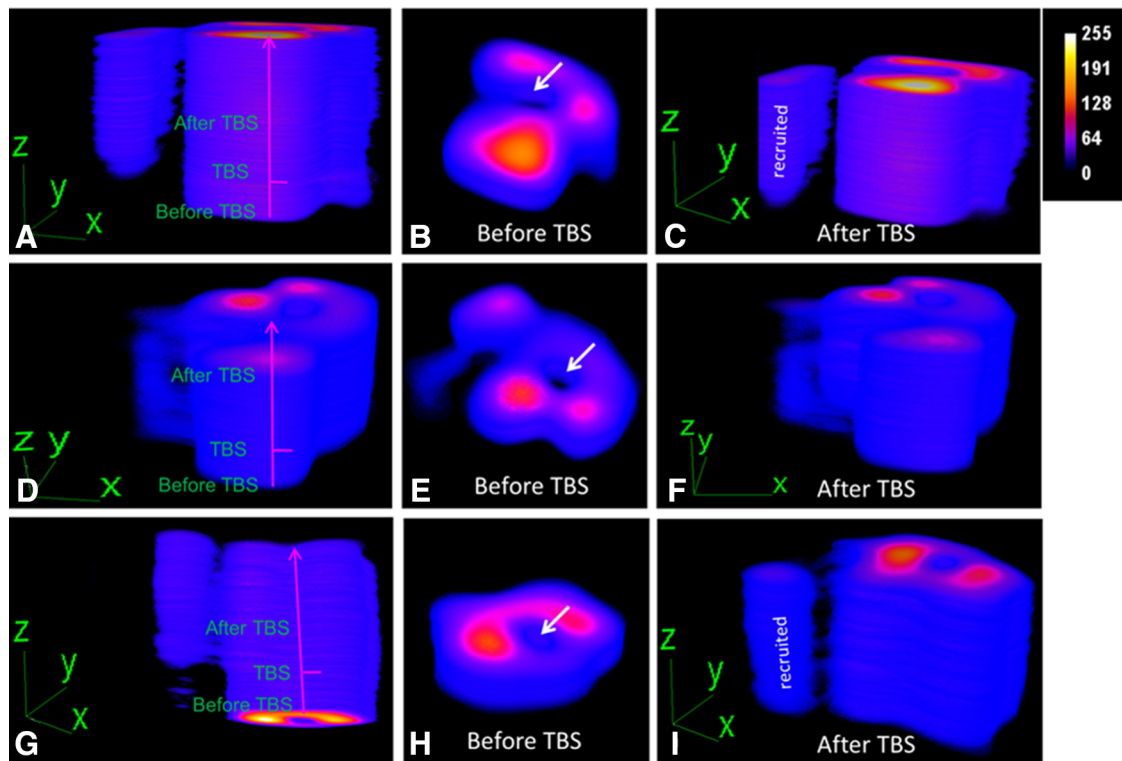


**Figure 9.** LTP induction evoked recruitment of cortical circuitry in WT and s831A mice. **A**, The spatiotemporal 3D volume showing the recruited responses after TBS in one sample slice from WT mice. The Z direction represented the whole recording procedure. **B**, **C**, The spatiotemporal distribution of the fEPSP before (**B**) and after (**C**) TBS split from **A**. **D–F**, The spatiotemporal 3D volume from one sample slice from s845A mice showed that TBS could not induce recruited responses. **G–I**, The spatiotemporal 3D volume showed the recruited responses after TBS in one sample slice from s831A mice.

recording system, we showed that TBS applied at one site in the ACC produces L-LTP within most of the recording sites in the WT and s831A mice, but not in the s845A mice. We also developed novel software for quantitative analysis and meaningful visualization that enhanced the spatial accuracy to the level of micros for the fEPSP signals in reconstructed high-resolution spaces. We thus computed accurate and quantitative information including dynamic location and the distribution of multiple fEPSP peaks and the network LTP in temporal (1D) and spatial (2D) dimensions.

The roles of phosphorylation of GluA1 for LTP have been investigated in the hippocampus. After the induction of hippocampal LTP, the expression of phosphorylated GluA1 at s831 and s845 sites is increased in the hippocampal CA1 (Barria et al., 1997; Mammen et al., 1997). Activation of CaMKII and PKC phosphorylates the s831 site of the GluA1 (Lee et al., 2000), which increases channel conductance of AMPARs and directly leads to LTP expression (Benke et al., 1998; Derkach et al., 1999). PKA phosphorylation of the s845 site of the GluA1, however, mainly contributes to AMPAR trafficking to the plasma membrane (Esteban et al., 2003; Oh et al., 2006). Phosphorylation of GluA1 at s831 or s845 lowers the threshold for LTP induction (Makino et al., 2011), while there are significant LTP deficits in s831 and s845 double-mutant mice (Lee et al., 2003), indicating that the phosphorylated s831 and s845 sites of GluA1 both play important roles for the hippocampal LTP. However, unlike the hippocampus, we found that the AC1–cAMP–PKA pathway rather than the PKC pathway is much more involved with synaptic potentiation in the ACC (Zhuo, 2008; Bliss et al., 2016; Zhuo, 2016). In cingulate pyramidal cells, LTP induced by TBS or pairing stimulation is abolished in AC1 knock-out mice or by AC1 inhibitor NB001

(Liau et al., 2005; Wang et al., 2011). By contrast, hippocampal CA1 LTP was not affected by AC1 deletion or NB001 application (Wang et al., 2011). These results indicate that signaling pathways for LTP in central synapses (hippocampus vs cingulate) are different. Such a difference actually provides a unique view for future clinical manipulations such as inhibiting chronic pain with fewer cognitive side effects or enhancing cognition without increasing chronic pain.

In animal models of acute inflammatory or neuropathic pain, the elevated density and activity of PKA-phosphorylated GluA1 at s845 has been reported (Xu et al., 2008; Bie et al., 2011; Chen et al., 2014a,c). Phosphorylation of GluA1 s845 sites likely contributes to behavioral sensitization, since both enhanced synaptic potentiation and behavioral hyperalgesia are greatly inhibited in s845 but not s831 mutant mice (Zhuo, 2008; Chen et al., 2014a,c). Nerve injury-induced overexpression of Ca<sup>2+</sup>-permeable AMPARs (CP-AMPARs) depends on the activation of PKA, and CP-AMPA inhibitor NASPM reverses ACC LTP (Chen et al., 2014c). In the present study, we further confirmed that PKA phosphorylation at s845 but not PKC phosphorylation at s831 of GluA1 is important for LTP in the ACC. Therefore, unlike the hippocampus, we propose that, in the ACC, PKA but not CaMKII/PKC phosphorylation of GluA1 is required for the expression of LTP. One possible reason is that the expression of LTP in the ACC depends on membrane AMPAR trafficking but not on the increased channel conductance. This prediction is supported by our previous findings that peripheral nerve injury mainly increases the number of membrane AMPARs but not the channel conductance in the ACC (Li et al., 2010; Chen et al., 2014c). Activation of PKA and increased postsynaptic CP-AMPA on the membrane may contribute to AMPAR trafficking in the ACC. In addition, it is pos-

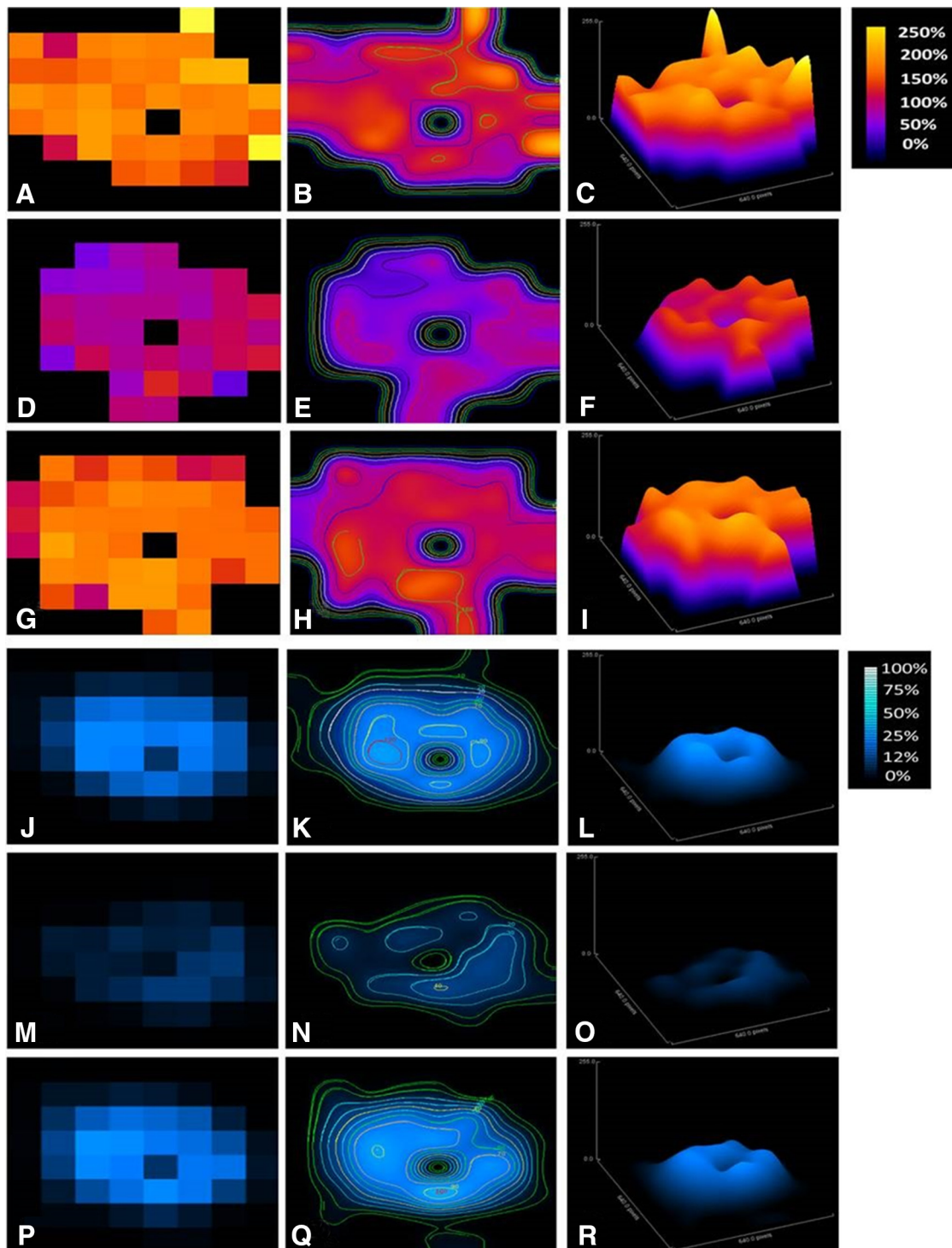


**Figure 10.** The probability distribution of the spatial strength and spatial frequency network L-LTP. **A–C**, The probability distributions of the averaged fEPSP slope (spatial strength) were from channels with L-LTP in WT mice. The originally acquired  $8 \times 8$  dataset (**A**) reconstructed ( $640 \times 640$ ) 2D signals (**B**) and 3D signals (**C**) were shown respectively. **D–F**, The probability distributions of the averaged fEPSP slope (spatial strength) were from channels with L-LTP in s845A mice. **G–I**, The probability distributions of the average fEPSP slope (spatial strength) were from channels with L-LTP in s831A mice. **J–L**, Probability distributions of averaged frequency of network L-LTP (spatial frequency) in WT mice (**J–L**), s845A mice (**M–O**), and s831A mice (**P–R**).  $n = 15$  slices in each type of mouse.

sible that CaMKII/PKC-phosphorylated s831 of GluA1 in the ACC may contribute to other forms of plasticity such as long-term depression (LTD). In the visual cortex, it has been reported that associative LTD requires the involvement of PKC activation (Seol et al., 2007). Future experiments are clearly needed to address this possibility.

Another interesting finding is that LTP induction recruited cortical circuitry in the WT and s831A mice but largely diminished such circuitry in the s845A mice. The recruitment of synaptic responses may be caused by the enhancement of presynaptic glutamate release, silent synapses, or postsynaptic trafficking of AMPAR (Chen et al., 2014b). Since the basal synaptic transmis-

sion is not changed in the three types of adult mice, we think the postsynaptic trafficking of AMPAR may have a more important role for the recruitment of synaptic responses. Some researchers have found that LTP induction promotes the GluA1 surface expression in spines and dendrites through PKA phosphorylation of GluA1 at the s845 site (Esteban et al., 2003; Oh et al., 2006; Henley and Wilkinson, 2016). This is likely the main reason for the recruited responses in our present work. The deficiency of recruitment in s845A mice is largely due to the inactive PKA pathway that failed to induce AMPAR surface trafficking.

In our research, by using the MED64 system, the LTP was recorded from multiple channels in one ACC slice. Comparing this to traditional two-electrode (one stimulation and one recording electrode) methods, this system helps to deepen our understanding of the multiple activated responses and signal spread. However, the spatial distribution of the real network response is limited by the low resolution of the recording channels. The temporal change of the signals is also hard to analyze. By the unbiased quantitative analysis, the number, shape, and distribution of multiple peaks of fEPSP signals can be visually achieved with a smoother and more stable interpolation of the original signals. In graph theory, a graph in this context is made up of vertices, nodes, or points that are connected by edges, arcs, or lines. Here, we consider the peaks of fEPSPs as the nodes or vertices in a graph network. The connectivity between these vertices is visualized using the distributed contour lines of slopes. In this way, the bottleneck for accurate localization and distribution of network signals acquired from the low-resolution recording system has been conquered to a large extent. We can further compute multiple distributions of contour lines to visualize the probable spatial strength and spatial frequency properties of the network LTP. To our knowledge, our work is for the first time to apply this type of analyzing method to check the spatial-temporal properties of network signals and LTP. This is useful for revealing the cellular response, synaptic transmission, and drug effect at circuit level. However, there are still a lot of uncertainties for the underlying connectivity among multiple fEPSP peaks by using only electrophysiology data in spatiotemporal dimensions. In the future, we will extend our approach to reconstruct higher-fidelity and more meaningful network signals by combining, for example, electrophysiology, morphology, and imaging information. In this way, we may reveal the underlying relationships for the connectivity and spatial-temporal changes of the network signals.

In summary, our results demonstrated that the PKA phosphorylation site of the GluA1 is important for the network LTP and recruitment of cortical circuitry in the ACC. Since ACC is important for the process of chronic pain, this PKA site of GluA1 may serve as a new target to inhibit the chronic pain. Further studies would investigate the detection of the relationship between pairwise channels before and after TBS, as well as expanded application such as the possible changed spatial-temporal properties of network LTP in chronic pain.

## References

- Anggono V, Huganir RL (2012) Regulation of AMPA receptor trafficking and synaptic plasticity. *Curr Opin Neurobiol* 22:461–469. [CrossRef Medline](#)
- Barria A, Derkach V, Soderling T (1997) Identification of the Ca<sup>2+</sup>/calmodulin-dependent protein kinase II regulatory phosphorylation site in the alpha-amino-3-hydroxyl-5-methyl-4-isoxazole-propionate-type glutamate receptor. *J Biol Chem* 272:32727–32730. [CrossRef Medline](#)
- Benke TA, Lüthi A, Isaac JT, Collingridge GL (1998) Modulation of AMPA receptor unitary conductance by synaptic activity. *Nature* 393:793–797. [CrossRef Medline](#)
- Bie B, Brown DL, Naguib M (2011) Increased synaptic GluR1 subunits in the anterior cingulate cortex of rats with peripheral inflammation. *Eur J Pharmacol* 653:26–31. [CrossRef Medline](#)
- Bliss TV, Collingridge GL, Kaang BK, Zhuo M (2016) Synaptic plasticity in the anterior cingulate cortex in acute and chronic pain. *Nat Rev Neurosci* 17:485–496. [CrossRef Medline](#)
- Chen T, Koga K, Descalzi G, Qiu S, Wang J, Zhang LS, Zhang ZJ, He XB, Qin X, Xu FQ, Hu J, Wei F, Huganir RL, Li YQ, Zhuo M (2014a) Postsynaptic potentiation of corticospinal projecting neurons in the anterior cingulate cortex after nerve injury. *Mol Pain* 10:33. [CrossRef Medline](#)
- Chen T, Lu JS, Song Q, Liu MG, Koga K, Descalzi G, Li YQ, Zhuo M (2014b) Pharmacological rescue of cortical synaptic and network potentiation in a mouse model for fragile X syndrome. *Neuropsychopharmacology* 39:1955–1967. [CrossRef Medline](#)
- Chen T, Wang W, Dong YL, Zhang MM, Wang J, Koga K, Liao YH, Li JL, Budisantoso T, Shigemoto R, Itakura M, Huganir RL, Li YQ, Zhuo M (2014c) Postsynaptic insertion of AMPA receptor onto cortical pyramidal neurons in the anterior cingulate cortex after peripheral nerve injury. *Mol Brain* 7:76. [CrossRef Medline](#)
- Chen T, O'Den G, Song Q, Koga K, Zhang MM, Zhuo M (2014d) Adenylyl cyclase subtype 1 is essential for late-phase long term potentiation and spatial propagation of synaptic responses in the anterior cingulate cortex of adult mice. *Mol Pain* 10:65. [CrossRef Medline](#)
- Collingridge GL, Isaac JT, Wang YT (2004) Receptor trafficking and synaptic plasticity. *Nat Rev Neurosci* 5:952–962. [CrossRef Medline](#)
- Derkach V, Barria A, Soderling TR (1999) Ca<sup>2+</sup>/calmodulin-kinase II enhances channel conductance of alpha-amino-3-hydroxy-5-methyl-4-isoxazolepropionate type glutamate receptors. *Proc Natl Acad Sci U S A* 96:3269–3274. [CrossRef Medline](#)
- Esteban JA, Shi SH, Wilson C, Nuriya M, Huganir RL, Malinow R (2003) PKA phosphorylation of AMPA receptor subunits controls synaptic trafficking underlying plasticity. *Nat Neurosci* 6:136–143. [CrossRef Medline](#)
- Henley JM, Wilkinson KA (2016) Synaptic AMPA receptor composition in development, plasticity and disease. *Nat Rev Neurosci* 17:337–350. [CrossRef Medline](#)
- Kang SJ, Liu MG, Chen T, Ko HG, Baek GC, Lee HR, Lee K, Collingridge GL, Kaang BK, Zhuo M (2012) Plasticity of metabotropic glutamate receptor-dependent long-term depression in the anterior cingulate cortex after amputation. *J Neurosci* 32:11318–11329. [CrossRef Medline](#)
- Kristensen AS, Jenkins MA, Banke TG, Schousboe A, Makino Y, Johnson RC, Huganir R, Traynelis SF (2011) Mechanism of Ca<sup>2+</sup>/calmodulin-dependent kinase II regulation of AMPA receptor gating. *Nat Neurosci* 14:727–735. [CrossRef Medline](#)
- Lee HK, Barbarosie M, Kameyama K, Bear MF, Huganir RL (2000) Regulation of distinct AMPA receptor phosphorylation sites during bidirectional synaptic plasticity. *Nature* 405:955–959. [CrossRef Medline](#)
- Lee HK, Takamiya K, Han JS, Man H, Kim CH, Rumbaugh G, Yu S, Ding L, He C, Petralia RS, Wenthold RJ, Gallagher M, Huganir RL (2003) Phosphorylation of the AMPA receptor GluR1 subunit is required for synaptic plasticity and retention of spatial memory. *Cell* 112:631–643. [CrossRef Medline](#)
- Liauw J, Wu LJ, Zhuo M (2005) Calcium-stimulated adenylyl cyclases required for long-term potentiation in the anterior cingulate cortex. *J Neurophysiol* 94:878–882. [CrossRef Medline](#)
- Li XY, Ko HG, Chen T, Descalzi G, Koga K, Wang H, Kim SS, Shang Y, Kwak C, Park SW, Shim J, Lee K, Collingridge GL, Kaang BK, Zhuo M (2010) Alleviating neuropathic pain hypersensitivity by inhibiting PKMzeta in the anterior cingulate cortex. *Science* 330:1400–1404. [CrossRef Medline](#)
- Liu MG, Kang SJ, Shi TY, Koga K, Zhang MM, Collingridge GL, Kaang BK, Zhuo M (2013a) Long-term potentiation of synaptic transmission in the adult mouse insular cortex: multielectrode array recordings. *J Neurophysiol* 110:505–521. [CrossRef Medline](#)
- Liu MG, Koga K, Guo YY, Kang SJ, Collingridge GL, Kaang BK, Zhao MG, Zhuo M (2013b) Long-term depression of synaptic transmission in the adult mouse insular cortex in vitro. *Eur J Neurosci* 38:3128–3145. [CrossRef Medline](#)
- Makino Y, Johnson RC, Yu Y, Takamiya K, Huganir RL (2011) Enhanced synaptic plasticity in mice with phosphomimetic mutation of the GluA1 AMPA receptor. *Proc Natl Acad Sci U S A* 108:8450–8455. [CrossRef Medline](#)
- Malinow R, Malenka RC (2002) AMPA receptor trafficking and synaptic plasticity. *Annu Rev Neurosci* 25:103–126. [CrossRef Medline](#)

- Mammen AL, Kameyama K, Roche KW, Huganir RL (1997) Phosphorylation of the alpha-amino-3-hydroxy-5-methylisoxazole-4-propionic acid receptor GluR1 subunit by calcium/calmodulin-dependent kinase II. *J Biol Chem* 272:32528–32533. [CrossRef Medline](#)
- Oh MC, Derkach VA, Guire ES, Soderling TR (2006) Extrasynaptic membrane trafficking regulated by GluR1 serine 845 phosphorylation primes AMPA receptors for long-term potentiation. *J Biol Chem* 281:752–758. [CrossRef Medline](#)
- Seol GH, Ziburkus J, Huang S, Song L, Kim IT, Takamiya K, Huganir RL, Lee HK, Kirkwood A (2007) Neuromodulators control the polarity of spike-timing-dependent synaptic plasticity. *Neuron* 55:919–929. [CrossRef Medline](#)
- Song Q, Liu MG, Zhuo M (2015) Minocycline does not affect long-term potentiation in the anterior cingulate cortex of normal adult mice. *Mol Pain* 11:25. [CrossRef Medline](#)
- Wang H, Xu H, Wu LJ, Kim SS, Chen T, Koga K, Descalzi G, Gong B, Vadakkan KI, Zhang X, Kaang BK, Zhuo M (2011) Identification of an adenylyl cyclase inhibitor for treating neuropathic and inflammatory pain. *Sci Transl Med* 3:65ra63. [CrossRef Medline](#)
- Xu H, Wu LJ, Wang H, Zhang X, Vadakkan KI, Kim SS, Steenland HW, Zhuo M (2008) Presynaptic and postsynaptic amplifications of neuropathic pain in the anterior cingulate cortex. *J Neurosci* 28:7445–7453. [CrossRef Medline](#)
- Zhao MG, Toyoda H, Lee YS, Wu LJ, Ko SW, Zhang XH, Jia Y, Shum F, Xu H, Li BM, Kaang BK, Zhuo M (2005) Roles of NMDA NR2B subtype receptor in prefrontal long-term potentiation and contextual fear memory. *Neuron* 47:859–872. [CrossRef Medline](#)
- Zhuo M (2008) Cortical excitation and chronic pain. *Trends Neurosci* 31:199–207. [CrossRef Medline](#)
- Zhuo M (2016) Neural mechanisms underlying anxiety-chronic pain interactions. *Trends Neurosci* 39:136–145. [CrossRef Medline](#)
- Zhuo M, Wu G, Wu LJ (2011) Neuronal and microglial mechanisms of neuropathic pain. *Mol Brain* 4:31. [CrossRef Medline](#)